

3D Focused Ion Beam Sectioning of Zirconium Oxides in Zircaloy-4 for the Characterisation of Cracking

H. E. Weekes^{a,*}, S. Ortner^a, A. Qaisar^b, S. Lozano-Perez^c, K. Jurkschat^c

^aNational Nuclear Laboratory, Building D5, First Floor, Culham Science Centre, Abingdon, Oxfordshire, OX14 3DB

^bNational Nuclear Laboratory, Central Laboratory, Seascale, Cumbria, CA20 1PG

^cUniversity of Oxford, Department of Materials, Parks Road, Oxford, 3PH

Abstract

Sequential 2D sectioning and imaging using a dual-beam focused ion beam has been used to characterise the interconnectivity of cracks in oxidised Zircaloy-4. Evidence of vertical, or vertical-component, cracks have been observed in multiple oxides of different thicknesses. Such features are considered critical in the provision of a percolation path between the environment and first band of lateral cracks, in between the lateral bands of cracks and between the final band of lateral cracks and the metal/oxide interface. Given their limited occurrence, localised tensile surface strains have been considered a potential source of initiation of these cracks.

1. Introduction

Zirconium alloys are extensively used for fuel clad components in light water reactors. Various degradation processes can challenge the integrity of the zirconium clad and this study focuses on the process of oxidation. Corrosion of zirconium alloys has long been recognised as one of the most limiting factors to the high burn-up operation of fuel rods in light water reactors and thus a comprehensive understanding of the mechanisms governing oxidation is crucial. Oxidation of zirconium alloys, both out- and in-reactor, occurs by inward migration of oxygen ions through the oxide layer; oxide growth at the metal interface depends on the kinetics of the oxygen diffusion through this layer. The corrosion kinetics of zirconium and its alloys are often described by an initial pre-transition regime with an approximate power law [1–3], followed by a transition in kinetics. At this point a change in corrosion kinetics occurs due a breakdown in the protective nature of the oxide and the proposed formation of crack networks [4, 5]. These cyclic transitions are repeated until an accelerated, roughly linear, breakaway corrosion rate takes place. The mechanism controlling the formation of the in-plane cracks is understood to be result of tensile stresses generated orthogonal to the metal/oxide interface, particularly at highly undulating locations [6, 7]. However, given their relative orientation to the metal/oxide interface, these lateral cracks cannot, in isolation, provide the pathway for diffusing oxygen from the environment to the underlying porosity; nano-porosity and through-thickness cracks are two potential factors under consideration, however observations have been quite limited [8–12].

Gaining a comprehensive understanding of the mechanisms controlling the oxidation process is non-trivial. Like most degradation processes, oxidation occurs in 3D yet the majority of characterisation techniques only allow the acquisition of 2D data. The resolution and quality of 3D data obtained is normally reduced when compared to that obtained in 2D; however, advances in the focused ion beam (FIB) technique means this no longer needs to be the case. Sequential 2D sectioning and imaging using a dual-beam FIB instrument is able to produce 3D representations of microstructures in the 50 nm–20 μ m range with nanometre resolution. This technique has been used to characterise a number of different microstructures, including (i) nickel-based superalloys to quantitatively characterise grains and precipitate-level microstructural features [13], (ii) 304 stainless steel to understand the effect of applied stress and cold-work on surface oxidation [14], (iii) high pressure die-cast Mg alloys to characterise the interconnectivity of intermetallic particles [15] and (iv) the connectivity of oxide cracks in ZIRLOTM [9]. Complementary to the work carried out by Ni et al. in [9], this study aims to demonstrate the use of sequential 2D sectioning, imaging and 3D reconstruction to describe the network of cracks developed in oxides formed on Zircaloy-4 during corrosion and their potential role in the observed transitions in oxidation kinetics.

2. Experimental

2.1. Materials

The zirconium samples used for this work are recrystallisation annealed Zircaloy-4 plate. After the samples were polished and pickled (in a solution containing hydrofluoric acid in accordance with ASTM G2), the coupons

*Corresponding author.

Email address: hannah.weekes1@outlook.co.uk (H. E. Weekes)

Table 1: Zircaloy-4 oxide samples studied.

Oxide thickness, μm	Description
2.25	Around first transition
3.50	Second cycle
5.19	Third cycle

were oxidised in accordance with the process outlined in [12].

Oxide thicknesses were calculated from weight gain measurements using the established relationship approximating 15 mg.dm^{-1} of oxygen weight gain to $1 \mu\text{m}$ of oxide growth [16]. Values given are averages, since the local thickness of the oxide varies from one Zr grain to another. The samples selected for examination using 3D FIB sectioning are listed in Table 1 together with a description of their oxidation state. Figure 1 shows where these selected samples lie on the average oxide thickness versus oxidation time curve [12].

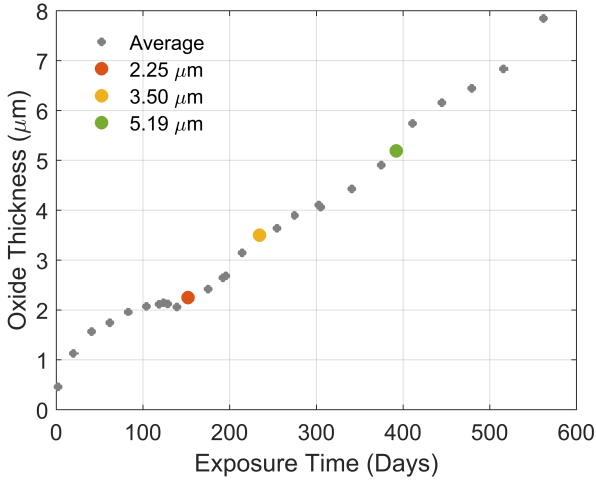


Figure 1: Location of analysed samples on the average oxide thickness versus oxidation time curve.

The location of the thinnest sample ($2.25 \mu\text{m}$ thick oxide) relative to first transition is not simple to define. Although its average oxide thickness is notably higher than the two preceding data points, these two points show a significant decrease in oxide thickness when compared to their previous data point and a fitted trend line (power or logarithmic) would place this sample late in the first oxidation cycle. It should be noted that the onset of transition will not be an instantaneous process across the whole sample; around transition there will be some regions of oxide still in cycle one and some which will have gone through transition. Therefore, this sample is considered to be ‘around first transition’. The second and third sample ($3.50 \mu\text{m}$ and $5.19 \mu\text{m}$ thick oxides) correspond to samples in the second cycle and third cycle respectively.

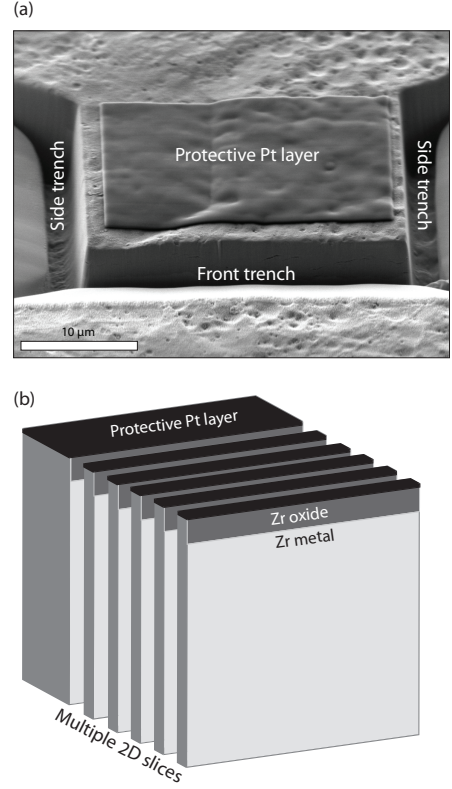


Figure 2: (a) Secondary electron beam image of the preparation for sectioning, angled at 54° showing the oxide-metal interface, (b) schematic of focussed ion beam sequential sectioning procedure.

2.2. FIB Sequential Sectioning and Imaging

Sample sectioning was carried out on a HELIOS NanoLab DualBeam Focused Ion Beam (FIB) and a Zeiss NVision 40 FIB instrument (2-30 kV Ga⁺ incident beam energy with currents of 700 pA). Higher magnification imaging was used to image nano-sized vertical cracks and the milling current was reduced to 300 pA. The samples were oriented with the focussed Ga⁺ ion beam normal to the sample surface and each slice was imaged using the secondary electron beam at a tilt angle of $52-54^\circ$. The sequential nature of the image capture process is shown in Figure 2. Before sectioning, a protective coating of Pt measuring approximately $20 \times 20 \mu\text{m}$ was deposited across the region of interest, see Figure 2a. One front and two side staircase trenches, also shown in Figure 2a, were milled at a current of 3.6 nA to minimise milling time. Lower currents were used to polish the sides of the region of interest; the curtaining effect (an artefact from FIB preparation whereby striations across the milling surface are formed) was reduced and the metal-oxide interface became visible. The front trench allowed the cross-sectional oxide to be imaged by the secondary electron beam and the side trenches provided regions onto which the milled material could be re-deposited. A beam current of 0.79 nA was used during sectioning with a step size of $\sim 100 \text{ nm}$ between each slice.

2.3. Data Reconstruction

Prior to reconstruction, sets of 2D images were stacked and aligned using Gatan Digital Micrograph. A refined drift correction was applied using a static feature on the non-milled sample surface common to all images to be reconstructed. Once aligned, a region of interest was selected from the stacked 2D slices and extracted to create a 3D dataset. The 3D reconstruction was carried out using the Avizo 6.1 programme. Cracks in the oxide and the interface between the Zr metal and oxide were defined using intensity thresholding. Automatic crack selection across multiple 2D slices was possible for the large cracks. However, given that the resolution limit of the cracks is heavily affected by their contrast against the oxide, lower contrast features, e.g. nano-scale cracks, were hard to define automatically. These features were either defined manually, or were not resolvable.

Overall, high resolution was achieved in the acquired images: 20 nm pixel size in the lower magnification images used for the reconstruction of lateral crack network and 5 nm pixel size in the higher magnification images used for smaller-scale investigations of through-thickness cracking.

3. Results

3.1. Lateral Crack Formation

Figure 3 shows the reconstructed 3D volumes of three samples, arranged in order of increasing oxide thickness. Figure 3a represents an oxide around the first transition (average thickness of $2.25\ \mu\text{m}$), Figure 3b an oxide part-way through the second cycle (average thickness of $3.50\ \mu\text{m}$) and Figure 3c an oxide in the third cycle of oxidation (average thickness of $5.19\ \mu\text{m}$). For all samples, the majority of the cracks lie parallel to the metal-oxide interface, particularly those lying closest to the metal/oxide interface. A lower density of smaller, more disconnected cracks are visible in the outer oxide (close to the environment/oxide interface), clearly shown in Figure 3a. For the second cycle ($3.50\ \mu\text{m}$) oxide, the connectivity of the lateral cracks is increased and an additional low density of lateral cracks appear close to the metal/oxide interface. The sample with the thickest oxide ($5.19\ \mu\text{m}$) is in its third oxidation cycle and two distinct bands of cracks are expected to be visible, coinciding with each cycle. Although two bands of lateral cracks can be seen in Figure 3c, the reconstructed oxide/metal interface shown in Figure 3d indicate the presence of multiple metal grains. These have been visually characterised by the significant change in metal/oxide interface profile. Given their proximity to the metal/oxide interface, the large lateral cracks in this sample are assumed to represent the second band of cracking, formed around the second transition in oxide kinetics. There are a number of reasons why the first band could not be visible in the reconstruction, including (i) this particular grain did not show significant levels of cracking

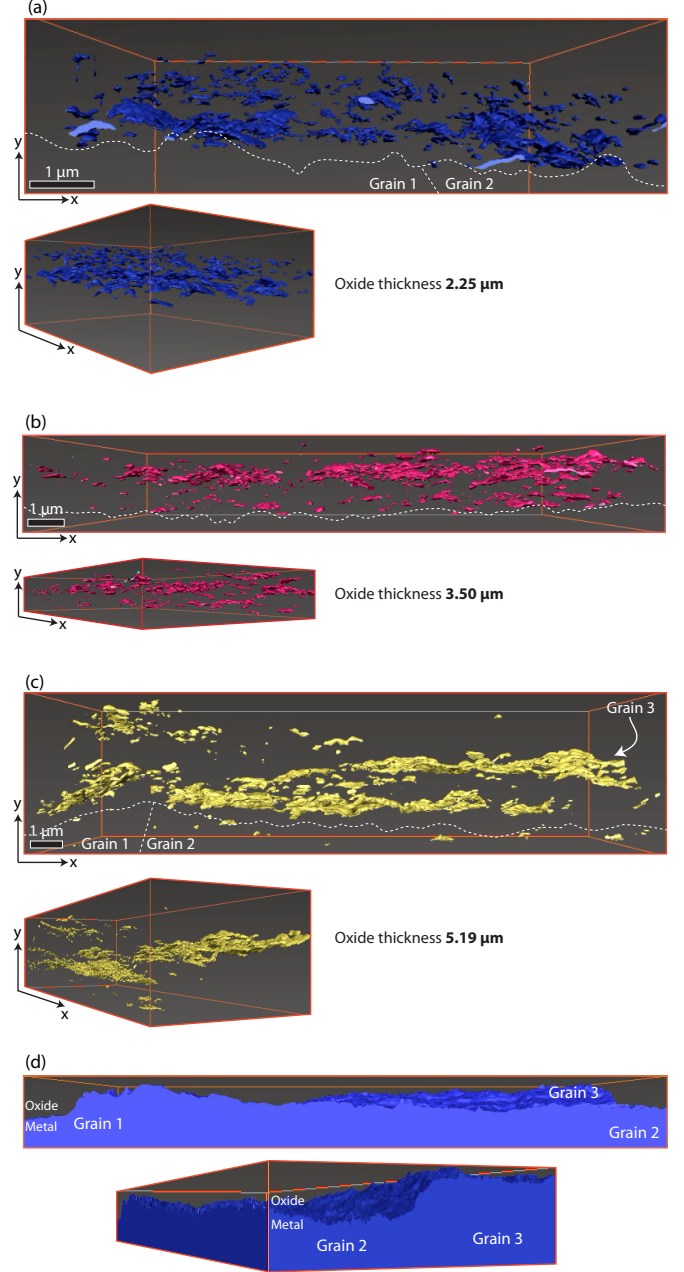


Figure 3: 3D reconstructions of crack networks for oxides of increasing thickness: (a) $2.25\ \mu\text{m}$ oxide (around first transition), (b) $3.50\ \mu\text{m}$ oxide (after first transition), (c) $5.19\ \mu\text{m}$ oxide (after second transition) and (d) variation in oxide thickness and lateral crack network across multiple grains. Oxide thickness: $5.19\ \mu\text{m}$.

around the first transition and/or (ii) the imaging conditions for this sample (contrast/focus/magnification) were not optimised to accurately threshold the cracks.

3.2. Vertical Crack Observations

Mid-way through acquisition of the $3.50\ \mu\text{m}$ oxide, a vertical feature appeared at the environment-oxide interface. Further investigation was carried out and a second set of 2D images were collected at a higher magnification

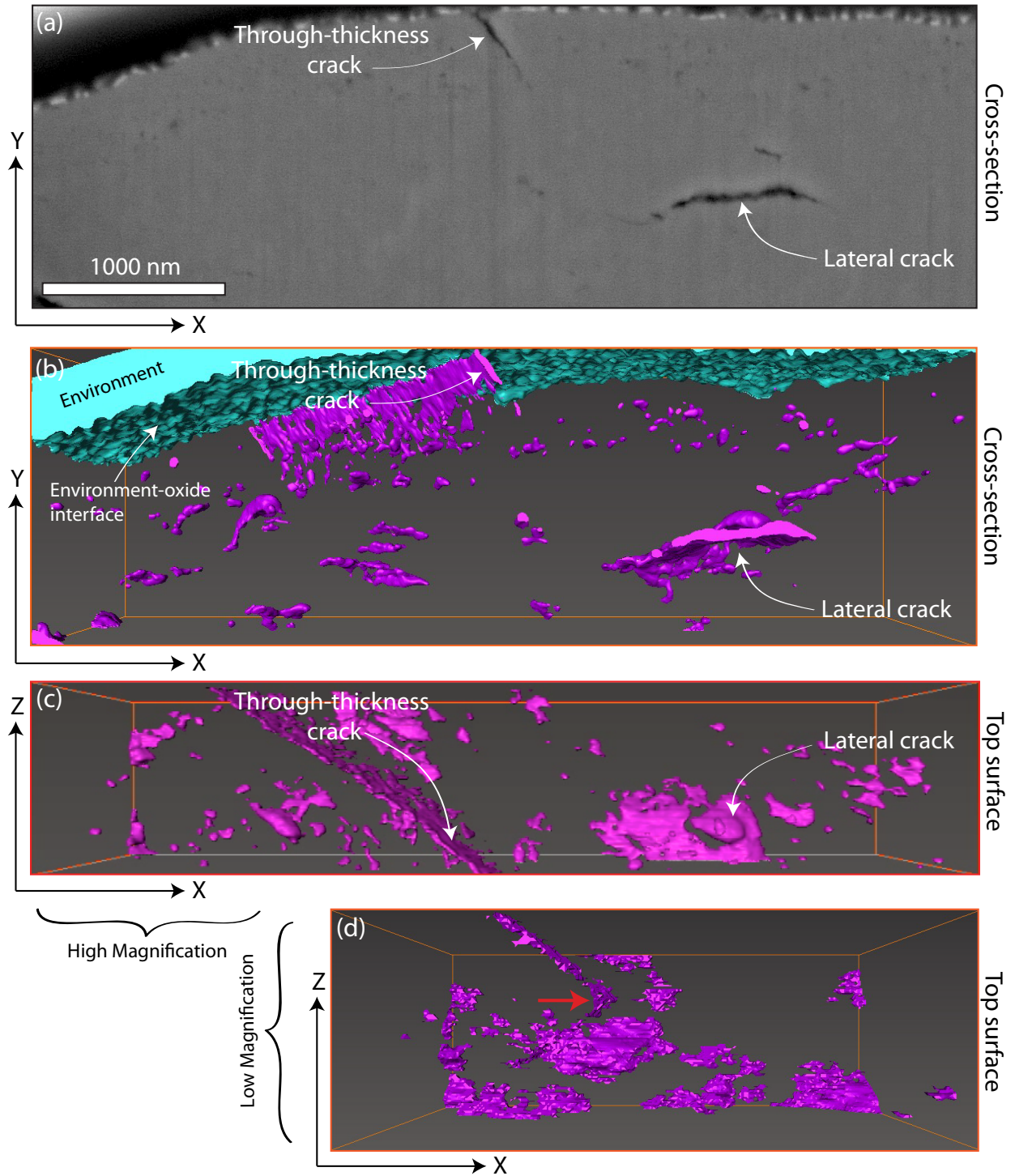


Figure 4: (a) Secondary electron beam image showing the cross-section of a 3.50 μm oxide with a through-thickness crack running inwards from the surface, (b-c) reconstructed 3D image of the oxide: side view (b) and top view (c). (d) represents a lower magnification reconstruction of the through-thickness crack viewed along the direction normal to the oxide surface (red arrow highlights sharp deviation in crack path). Colour code: pink - cracks, blue - environment-oxide interface.

(about 4 x larger). Figure 4a shows a single 2D SEM slice from this smaller dataset and identifies a through-thickness crack of approximately 500 nm in length running inwards from the sample surface.

The reconstructed 3D image of the cross-sectional oxide surrounding the through thickness crack is shown in Figure 4b-d. Figure 4d has been reconstructed from the lower magnification dataset and, although the resolution of these images is poorer than those used to create Figure 4b-c, it is able to provide further insight into the path of the crack across the sample surface. The through-thickness crack is visible in the equiaxed zone of the oxide (ranging ~ 200 nm in depth from the environment-oxide interface [17]) and is surrounded by fine intergranular cracks. Micro-scale lateral cracks are visible in the newer regions of the oxides. No connectivity between the vertical and lateral cracks is observed but this does not necessarily mean it has not occurred. A linear crack path along the sample surface is shown in Figure 4c and the lower magnification reconstruction (Figure 4d) shows a sharp deviation in the crack path, marked with a red arrow in Figure 4d. From the SEM cross-section images (Figure 5), taken at the beginning and end of the reconstruction, the vertical

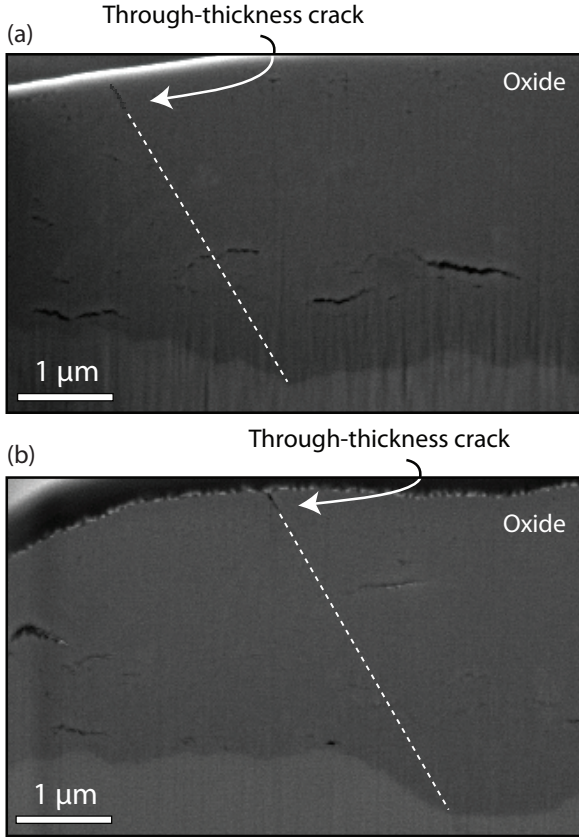


Figure 5: SEM images taken at the beginning (a) and end (b) of the higher magnification FIB sectioning focused around the vertical crack (highlighted) observed in the $3.50\ \mu\text{m}$ oxide.

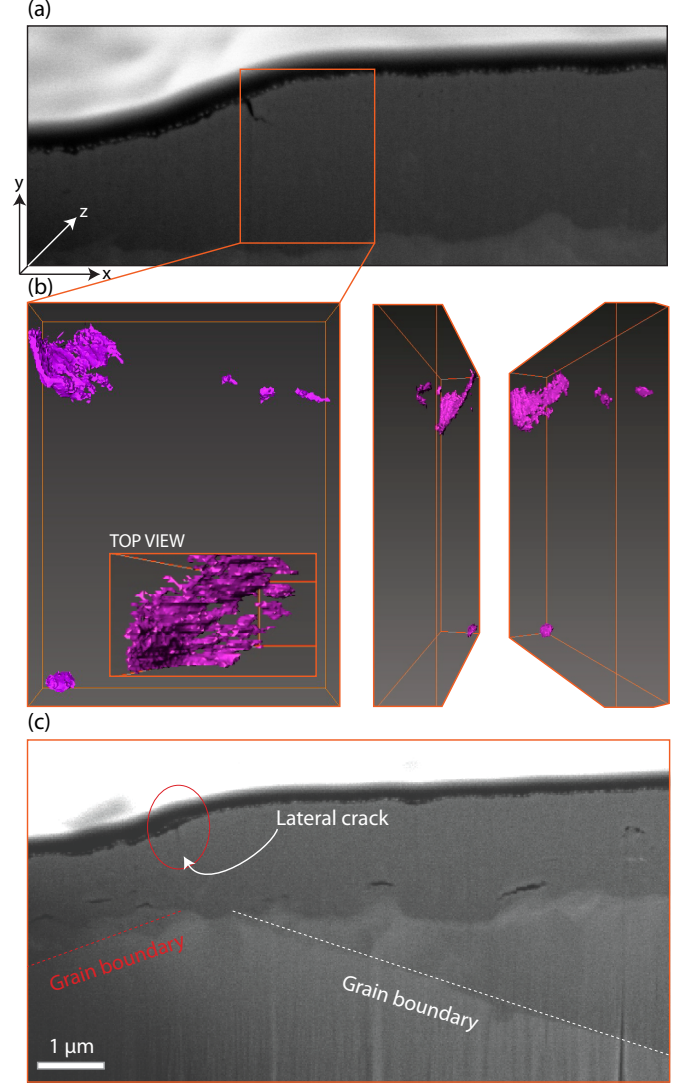


Figure 6: (s) SEM image showing the cross-section of a $2\ \mu\text{m}$ thick Zr oxide with a through-thickness crack-like feature running inwards from the surface. (b) 3D reconstruction of the crack imaged along the z-axis of the sample, see (a) for sample orientation. [inset: 3D view of crack along the y-axis]. (c) Grain boundary(ies) in Zr metal located below the through-thickness crack-like feature in the Zr oxide.

crack appears to be accompanied by a steep change in oxide thickness. This change in metal/oxide interface profile, and the change in crack path direction, could indicate that the crack is running along, or initiated from, a grain boundary.

Figure 6 shows a second surface breaking feature observed in a thinner, first cycle ($\sim 2.1\ \mu\text{m}$) oxide. Unfortunately, it was not possible to successfully reconstruct the full dataset but it has still been possible to gain some insight into the cracking behaviour of this sample. Figure 6a is a secondary electron image captured part-way through serial sectioning and shows a through-thickness crack-like feature of a few hundred nm running inwards

from the sample surface. This feature was identified using higher resolution sectioning and imaging from a reduced area. Figure 6b shows this feature viewed along the z-axis and, compared to the reconstructed vertical crack shown in Figure 4, it appears quite different. While Figure 4 is extremely linear in nature showing a sharp change in crack propagation path partway through (red arrow in Figure 4), this feature appears more curved. Figure 6c shows the Zr oxide and Zr metal surrounding the vertical crack and indicates the presence of a grain boundary, or potentially a triple point, in the metal below the vertical crack. Its presence on, or in the vicinity of, a grain boundary triple point may in fact account for its more disordered appearance.

Figure 7 provides examples of vertical-component cracks linking (or with the potential to link) lateral cracks together, observed in the second cycle oxide. These correspond to connectivity within a single band of lateral cracks or between two separate bands of lateral cracks. Figure 7(a) shows a through thickness crack linking two separate lateral cracks together. Figure 7(b) shows a large lateral cracks with an extended crack tip running, in part, close to vertical towards the metal/oxide interface.

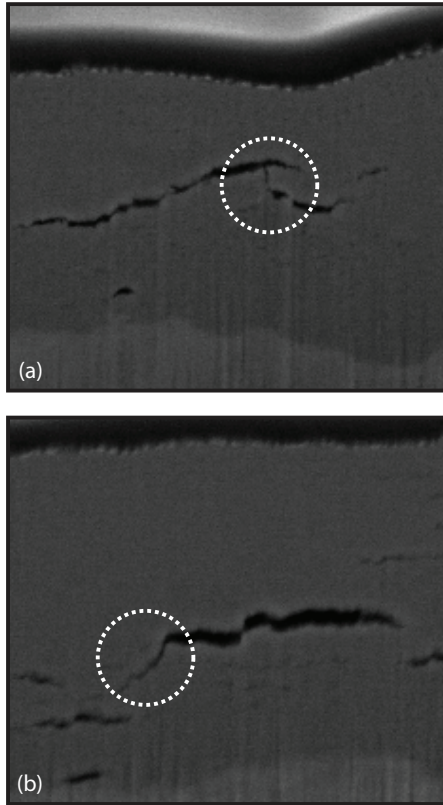


Figure 7: Observations of vertical-component cracks linking (or with the potential to link) lateral cracks. Taken from the second cycle (3.5 μm) oxide.

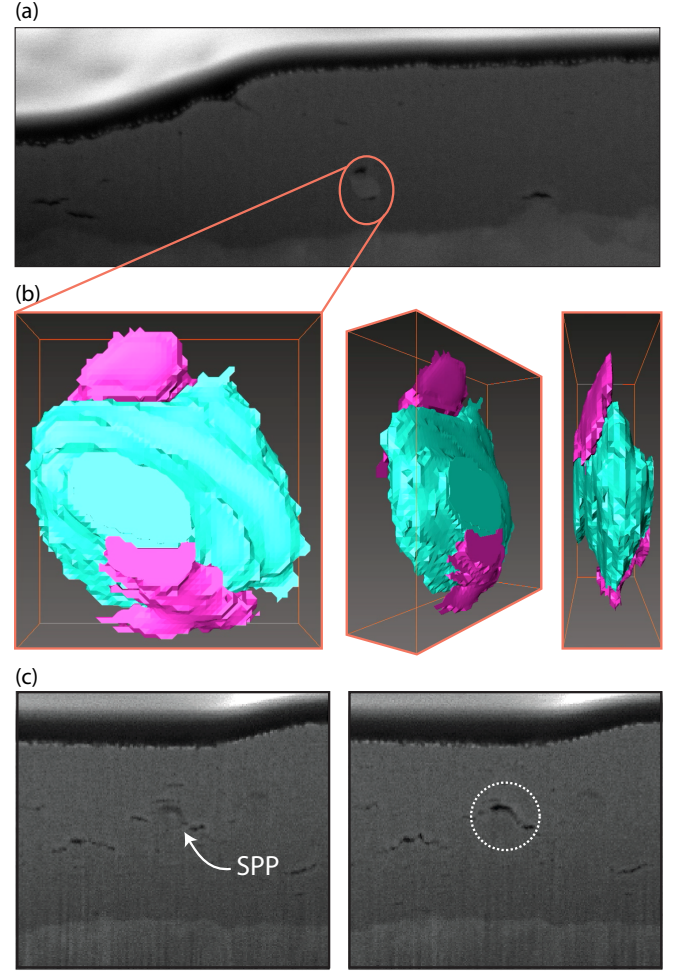


Figure 8: (a) SEM cross-section of Zr oxide showing location of SPP close to the metal/oxide interface, (b) reconstructed 3D image of cracks surrounding a secondary phase precipitate in a zirconium oxide around first transition and (c) evidence of cracking around an SPP. In the 3D reconstructions pink represents a crack and turquoise represents the SPP.

3.3. Effect of SPPs on Cracking

Data from the literature have shown a close relationship between crack formation and secondary phase particles (SPP) in zirconium oxides [6, 18–20] and a number of observations of cracking associated with SPPs in all oxides analysed has been shown in this study. Figure 8a shows a selected 2D image from an around first transition oxide (2.25 μm) and shows a propensity for cracks to nucleate both directly above and below an SPP. A 3D reconstruction of this SPP is given in Figure 8b and shows two cracks that have formed along the precipitate-matrix interface. Complementary to Figure 7 in Sub-Section 3.2 which gives evidence of vertical-component cracks away from the environment/oxide interface, Figure 8c shows a crack extending vertically around an SPP. This provides another potential source of connectivity between lateral cracks.

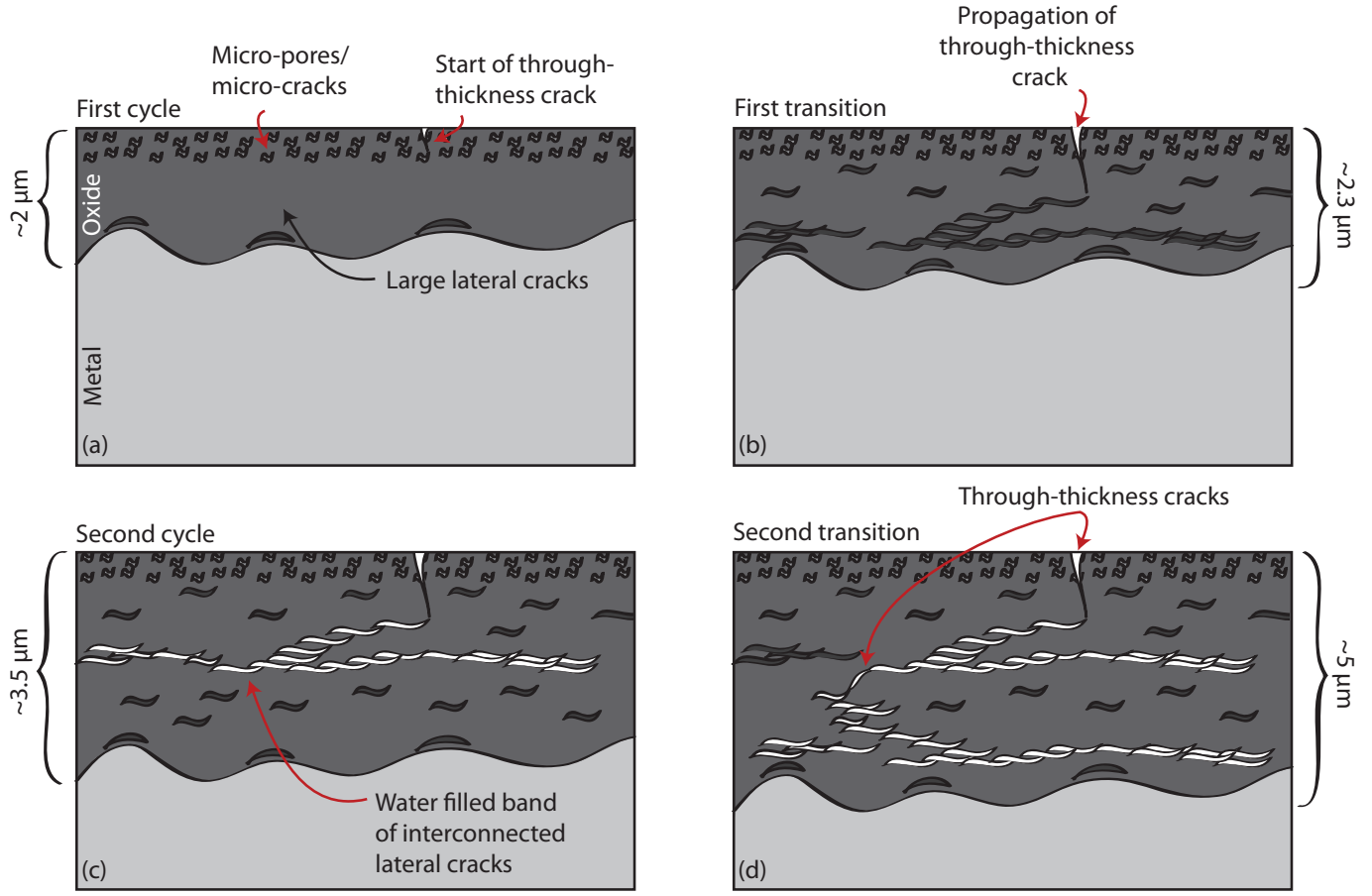


Figure 9: Schematic representation of proposed mechanisms for oxidation process leading to transition. (a) First cycle oxide, (b) post-transition (first cycle) oxide, (c) second cycle oxide and (d) post-transition (second cycle) oxide. The white cracks represent those filled with water.

4. Discussion

Cracks of different sizes are reported in zirconium alloy oxides and are often said to be correlated with the onset of transition, or a higher corrosion rate. The point at which cracks begin to initiate has been a subject of much debate over the years, with some researchers considering the transition in corrosion kinetics to be the point at which cracks form. This study, however, has shown clearly that new in-plane cracks are found mid-way through individual cycles, as are cracks running from the surface with a through-thickness component, indicating the steady formation of cracks throughout the entire corrosion cycle.

The majority of cracks observed in this study are oriented parallel to the oxide metal interface and cannot provide a through-thickness path for the environment. Tejland et al.[6] have suggested that oxygen could diffuse more rapidly along the periphery of the crack than through the bulk, allowing the lateral cracks to short-circuit the solid-state diffusion paths. Ni et al.[10] and Tupin et al.[21], however, consider that the lateral cracks should reduce the diffusion across the oxide by increasing the path length.

The balance between acceleration and deceleration will depend on the relative rates of bulk, grain boundary and surface diffusion and grain and crack size.

Very few observations of through-thickness cracking in the early stages of oxidation have been reported in the literature. Using high resolution secondary ion mass spectroscopy, Yardley et al.[8] showed a narrow vertical crack penetrating the majority of a sec on cycle oxide in low Sn ZIRLOTM. This has been considered by the authors as the direct path by which water is able to penetrate through the oxide in order to react with the underlying metal and increase the local oxidation rate. Ortner et al.[11] also observed through-plane cracking in Zircaloy-4, although their cracks were not found to connect to the first band of lateral cracks. Their cracks were oriented normal to the metal/oxide interface and indicate that they formed under tension. However, as mentioned previously, the transformation from Zr to Zr oxide causes high levels of compressive stress in the oxide, and synchrotron X-ray diffraction measurements have confirmed that the oxide remains, on average, in compression in the in-plane direction through several cycles of oxidation[12, 22].

Given the small number of observations of through-thickness cracks, it is possible that their formation should not be considered as a response to the average stress but as a response to a localised extreme in the stress distribution. Stress heterogeneities in the oxide could arise from a number of sources:

- i A heterogeneity in the distribution of remnant tetragonal oxide grains, and hence in the distribution of the strains produced by the martensitic monoclinic-tetragonal transformation[23–25];
- ii Steps in the metal-oxide interface at boundaries between metal grains oxidising at different rates[24, 26, 27];
- iii Metal grain-to-grain mismatches in strain caused by the anisotropic nature of the elastic and yield properties of Zr alloys as they undergo the creep induced by oxidation[11, 28–30].

Ni et al.[9] suggested that through-thickness cracks formed as a result of the increasing density of grain boundary pores in the oxide. As with option (i) above, this mechanism would not favour the prior metal grain boundaries as through-thickness crack sites. Nevertheless, pores in the oxide grain boundaries or micro cracks formed by transformation stresses could aid the growth of cracks formed at the sites of stress localisation’s produced by options (ii) or (iii). A schematic representation of the proposed mechanism developed for the oxidation process leading up to transition is given in Figure 9. Oxidation occurs via the inward diffusion of oxygen, unbalanced by the outward diffusion of zirconium. As a result, there is a volume expansion, producing elastic compressive stresses in the oxide, and corresponding elastic/plastic tension in the metal substrate. The initial average rate of oxidation will be fast, but will reduce as the oxide thickens and the diffusion distance extends. Any locally higher oxidation rates along the metal/oxide interface (perhaps where oxide grain boundaries meet the metal/oxide interface) will produce a protrusion. The oxide in the protrusion can relax sideways, relaxing its stored strain energy, but suppressing nearby oxide growth. This will stabilise the protrusion against the tendency of the interfacial energy to flatten the metal/oxide interface, and produce an undulating corrosion front. Under the action of the overall in-plane compressive stress this produces tensile out-of-plane stresses at delays in the oxide front (the less deeply oxidising regions) and compressive out-of-plane stresses behind the protrusions [7, 31]. Similar considerations can also be made when explaining the formation of cracks at the interfaces of SPPs, Figure 8. SPPs are incorporated in the oxide film in metallic form and have an oxidation rate that is generally slower than that of the Zr metal matrix [32, 33]. Their eventual oxidation will be accompanied by a volume expansion, with the Zr oxide sustaining a tensile stress by the compressive constraint of the SPPs, and will produce an

additional local stress in the oxide which is relieved by the formation of these cracks[18].

The cracks that form at the delays in the oxidation front do not initially extend as their tips run into compressive regions behind the protrusions but, as the oxidation front moves further into the metal, so do the stress fields associated with the undulations. The lateral cracks become subject to the longer-range out-of-plane stress [12] and the influence of neighbouring cracks, extend and interlink to produce the rafts observed in Figure 3. The rafts appear to be interlinked over the area of at least a metal grain. Such wide rafts are more likely to reduce the solid state flux of oxygen through the oxide than to accelerate it.

Acceleration of the oxidation rate requires access of the environment closer to the oxide/metal interface. Given the observations shown in this study, the through-thickness, vertical cracks will play a key role in this process. Referring to Figure 9, the formation of a single through-thickness crack can provide the link between the environment and an entire raft of interconnected lateral cracks (the locations at which the through-thickness cracks form is likely to be controlled by the underlying Zr metal, although for simplicity this is not demonstrated in Figure 9. This will allow water to percolate through the oxide, filling up the lateral cracks close to the metal/oxide interface and the oxide ceases to function as an effective barrier. A new, very thin barrier layer is formed and a new cycle begins with an initially fast corrosion rate.

It is recognised that the through-thickness cracks observed in this study are not shown to fully connect the environment to the first layer of interconnected lateral cracks or, for the thicker oxides, to the final layer of cracks to the metal/oxide interface. There could be a number of reasons for this: firstly, we may be viewing through-thickness cracks which have initiated but not propagated, perhaps because of the presence of triple points; secondly, the cracks may be very fine, at the resolution limit of the analytical methodology presented in this study. In this case, the actual crack tips may be deeper into the oxide than observed in Figure 4-Figure 6. In support of the latter suggestion, Figure 10 shows high resolution transmission electron microscopy (TEM) images of the first cycle oxide (2.25 μm). It shows a number of fine cracks branching from the wider tip of a lateral crack tip. It is considered likely that these features will contribute to the connectivity of the crack network, but will likely not be resolvable at the magnifications required for the 3D FIB sectioning technique.

Conclusions

This study used high resolution 2D imaging and 3D reconstruction to characterise oxide cracking in Zircaloy-4 at different points in the corrosion process; first, second and third cycle Zr oxides were investigated. It has shown the steady formation of, predominantly, in-plane (lateral)

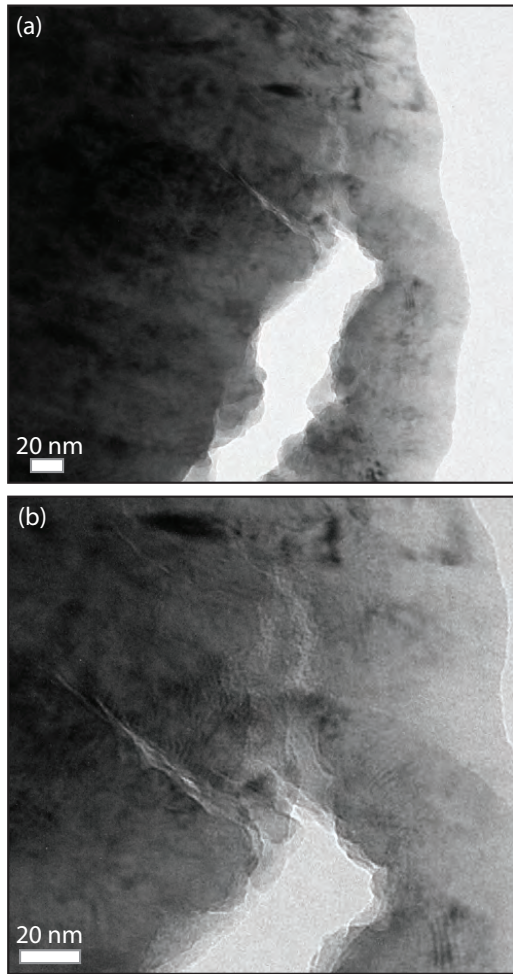


Figure 10: Bright-field TEM micrographs of 2.25 μm thick oxide showing propagation of multiple nano-scale cracks not visible in the 3D reconstructions.

cracks throughout the entire corrosion cycle. The connectivity of these cracks increases and this extensive interconnectivity is a key stage towards transition.

Cracks with a mainly through-thickness (vertical) component have been observed in a number of oxides of different thicknesses. Such features could provide the required percolation path between the environment and the first band of lateral cracks and between the final band of lateral cracks and the metal/oxide interface. On the basis of the observations here, the rafts of interconnected lateral cracks form before the vertical cracks grow in from the surface in Zircaloy-4. The sequence may differ in different alloys. In either case, the connectivity of the lateral cracks means very few vertical cracks are required to bring the environment close to the metal/oxide interface over wide areas. The conditions to form a vertical crack thus need not pertain over the entire oxidising surface, but only at a few locations.

The formation of vertical cracks will likely occur under local tension. Strain mismatches at grain boundaries in

the creeping metal substrate or stress concentrations at steps in the metal/oxide interface have been considered as possible sources of such local tensile conditions.

Acknowledgements

The authors recognise the contributions of Wood plc. for the provision of material for this study.

References

- [1] T. Arima, K. Moriyama, N. Gaja, H. Furuya, K. Idemitsu, Y. Inagaki, Oxidation kinetics of Zircaloy-2 between 450 C and 600 C in oxidizing atmosphere, *Journal of nuclear ...* (1998) 67–77.
- [2] A. Yilmazbayhan, A. T. Motta, R. J. Comstock, G. P. Sabol, B. Lai, Z. Cai, Structure of zirconium alloy oxides formed in pure water studied with synchrotron radiation and optical microscopy: relation to corrosion rate, *Journal of nuclear ...* (2003) 6–22.
- [3] B. Cox, Some thoughts on the mechanisms of in-reactor corrosion of zirconium alloys, *Journal of nuclear ...* (2004) 331–368.
- [4] B. Cox, Processes occurring during the breakdown of oxide films on zirconium alloys, *Journal of nuclear ...* (1968) 50–66.
- [5] D. H. Bradhurst, P. M. Heuer, The influence of oxide stress on the breakaway oxidation of Zircaloy-2, *Journal of nuclear ...* (1970) 35–47.
- [6] P. Tejlund, H.-O. Andren, Origin and effect of lateral cracks in oxide scales formed in zirconium alloys, *Journal of nuclear ...* 430 (1-3) (2012) 64–71.
- [7] M. Parise, O. Sicardy, G. Cailletaud, Modelling of the mechanical behaviour of the metal-oxide system during Zr alloy oxidation, *Journal of nuclear ...* (1998) 35–46.
- [8] S. S. Yardley, K. L. Moore, N. Ni, J. F. Wei, S. Lyon, M. Preuss, S. Lozano-Perez, C. R. M. Grovenor, An investigation of the oxidation behaviour of zirconium alloys using isotopic tracers and high resolution SIMS, *Journal of Nuclear Materials* 443 (1-3) (2013) 436–443.
- [9] N. Ni, S. Lozano-Perez, J. M. Sykes, G. D. W. Smith, C. R. M. Grovenor, Focussed ion beam sectioning for the 3D characterisation of cracking in oxide scales formed on commercial ZIRLO alloys during corrosion in high temperature pressurised water, *Corrosion Science* (2011) 4073–4083.
- [10] N. Ni, S. Lozano-Perez, M. L. Jenkins, C. English, G. D. W. Smith, J. M. Sykes, C. R. M. Grovenor, Porosity in oxides on zirconium fuel cladding alloys, and its importance in controlling oxidation rates, *Scripta Materialia* 62 (8) (2010) 564–567.
- [11] S. Ortner, H. Swan, A. LaFerrere, C. English, J. M. Hyde, P. D. Styman, K. Jurkschat, H. Hulme, A. Pantelli, M. Gass, V. Allen, P. Frankel, Study of Zircaloy corrosion to develop mechanistic understanding, in: *Fontevraud 8 - Contribution of Materials Investigations and Operating Experience to LWR's Safety, Performance and Reliability*, 2014.
- [12] H. Swan, M. S. Blackmur, J. M. Hyde, A. LaFerrere, S. Ortner, P. D. Styman, C. Staines, M. Gass, H. Hulme, A. Cole-Baker, P. Frankel, The measurement of stress and phase fraction distributions in pre and post-transition Zircaloy oxides using nano-beam synchrotron X-ray diffraction, *Journal of nuclear ...* (2016) 559–575.
- [13] M. D. Uchic, M. A. Groeber, D. M. Dimiduk, J. P. Simmons, 3D microstructural characterisation of nickel superalloys via serial-sectioning using a dual beam FIB-SEM, *Scripta Materialia* (2006) 23–28.
- [14] S. Lozano-Perez, K. Kruska, I. Iyengar, T. Terachi, T. Yamada, The role of cold work and applied stress on surface oxidation of 304 stainless steel, *Corrosion Science* (2011) 78–85.

- [15] A. V. Nagasekhar, C. H. Caceres, C. Kong, 3D characterisation of intermetallics in a high pressure die cast Mg alloy using focused ion beam tomography, *Materials Characterisation* (2010) 1035–1042.
- [16] A. Nechaev, Corrosion of zirconium alloys in nuclear power plants, Tech. Rep. IAEA-TECDOC-684, Vienna (Jan. 1993).
- [17] A. Garner, A. Gholinia, P. Frankel, M. Gass, I. MacLaren, M. Preuss, The microstructure and microtexture of zirconium oxide films studied by transmission electron backscatter diffraction and automated crystal orientation mapping with transmission electron microscopy, *Acta Materialia* (2014) 159–171.
- [18] J. Huang, M.-y. Yao, C.-y. Gao, X. Liang, J.-c. Peng, J.-l. Zhang, B.-x. Zhou, *Corrosion Science*, *Corrosion Science* 99 (2015) 172–177.
- [19] B. de Gabory, A. T. Motta, K. Wang, Transmission electron microscopy characterisation of Zircaloy-4 and ZIRLO oxide layers, *Journal of nuclear* . . .
- [20] K. Annand, M. Nord, I. MacLaren, M. Gass, The corrosion of $\text{Zr}(\text{Fe},\text{Cr})_2$ and Zr_2Fe secondary phase particles in Zircaloy-4 under 350C pressurised water conditions, *Corrosion Science* (2017) 213–223.
- [21] M. Tupin, M. Pijolat, F. Valdivieso, M. Soustelle, A. Frichet, P. Barberis, Differences in reactivity of oxide growth during the oxidation of Zircaloy-4 in water vapour before and after the kinetic transition, *Journal of Nuclear Materials* 317 (2-3) 130–144.
- [22] E. Polatidis, P. Frankel, J. Wei, M. Klaus, R. J. Comstock, A. Ambard, S. Lyon, R. A. Cottis, M. Preuss, Residual stresses and tetragonal phase fraction characterisation of corrosion tested Zircaloy-4 using energy dispersive synchrotron X-ray diffraction, *Journal of nuclear* . . . (2012) 102–112.
- [23] P. Rudling, G. Wikmark, A unified model of Zircaloy BWR corrosion and hydriding mechanisms , *Journal of nuclear* . . .
- [24] S. Taniguchi, Stresses developed during the oxidation of metals and alloys, *Transactions ISIJ*.
- [25] P. Platt, P. Frankel, M. Gass, R. Howells, M. Preuss, Finite element analysis of the tetragonal to monoclinic phase transformation during oxidation of zirconium alloys, *Journal of Nuclear Materials* (1-3) (2014) 290–297.
- [26] R. A. Ploc, Transmission electron microscopy of thin (≈ 2000 Å) thermally formed ZrO_2 films, *Journal of Nuclear Materials* (1968) 48–60.
- [27] H. G. Kim, T. H. Kim, Y. H. Jeong, Oxidation characteristics of basal (0002) plane and prism (11-20) plane in HCP Zr, *Journal of Nuclear Materials* (2002) 44–53.
- [28] P. Tejlund, H.-O. Andren, Oxidation induced localized creep deformation in Zircaloy-2, *Journal of Nuclear Materials* (13) 30–34.
- [29] P. Barberis, V. Rebeyrolle, J. J. Vermoyal, V. Chabretou, J. P. Vassault, CASTA DIVA: Experiments and modelling of oxide-induced deformation in nuclear components, *Journal of ASTM International* 5 (5) (2008) 612–630.
- [30] M. Blat-Yrieix, A. Ambard, F. Fact, A. Miquet, S. Beguin, N. Cayet, Toward a better understanding of dimensional changes in Zircaloy-4: What is the impact induced by hydrides and oxide layer?, *Journal of ASTM International* 5 (9) (2008) 594–609.
- [31] N. Vermaak, G. Parry, R. Estevez, Y. Bréchet, New insight into crack formation during corrosion of zirconium-based metal-oxide systems, *Acta Materialia* (2013) 4374–4383.
- [32] C. Proff, S. Abolhassani, C. Lemaignan, *Journal of Nuclear Materials*, *Journal of Nuclear Materials* 432 (1-3) (2013) 222–238.
- [33] C. Proff, S. Abolhassani, C. Lemaignan, *Journal of Nuclear Materials*, *Journal of Nuclear Materials* 416 (1-2) (2011) 125–134.